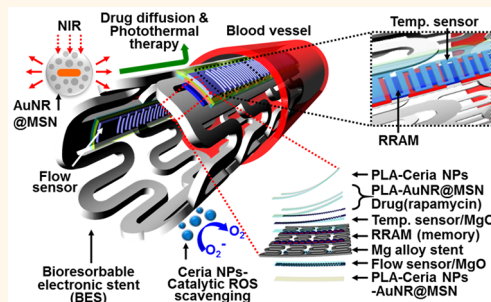


Bioresorbable Electronic Stent Integrated with Therapeutic Nanoparticles for Endovascular Diseases

Donghee Son,^{†,‡,○} Jongha Lee,^{†,‡,○} Dong Jun Lee,^{†,‡,○} Roozbeh Ghaffari,[§] Sumin Yun,^{||} Seok Joo Kim,^{†,‡} Ji Eun Lee,^{†,‡} Hye Rim Cho,^{†,‡} Soonho Yoon,[‡] Shixuan Yang,[#] Seunghyun Lee,[‡] Shutao Qiao,[#] Daishun Ling,[▽] Sanghun Shin,^{†,‡} Jun-Kyul Song,^{†,‡} Jaemin Kim,^{†,‡} Taeho Kim,^{†,‡} Hakyong Lee,^{†,‡} Jonghoon Kim,^{†,‡} Min Soh,^{†,‡} Nohyun Lee,^{||} Cheol Seong Hwang,[□] Sangwook Nam,^{||} Nanshu Lu,[#] Taeghwan Hyeon,^{*,†,‡} Seung Hong Choi,^{*,†,‡} and Dae-Hyeong Kim^{*,†,‡}

[†]Center for Nanoparticle Research, Institute for Basic Science (IBS), Seoul 151-742, Republic of Korea, [‡]School of Chemical and Biological Engineering and Institute of Chemical Processes, Seoul National University, Seoul 151-742, Republic of Korea, [§]MC10 Inc., 9 Camp Street, Cambridge, Massachusetts 02140, United States, ^{||}School of Electrical and Computer Engineering and INMC, Seoul National University, Seoul 151-742, Republic of Korea, [‡]Department of Radiology, Seoul National University College of Medicine, Seoul 110-744, Republic of Korea, [#]Center for Mechanics of Solids, Structures and Materials, Department of Aerospace Engineering and Engineering Mechanics, Texas Materials Institute, University of Texas at Austin, 210 E. 24th Street, Austin, Texas 78712, United States, [▽]Institute of Pharmaceuticals, College of Pharmaceutical Sciences, Zhejiang University, 866 Yuhangtang Road, Hangzhou 310058, China, ^{*}School of Advanced Materials Engineering, Kookmin University, Seoul 136-702, Republic of Korea, and [□]Department of Materials Science and Engineering and Inter-university Semiconductor Research Center, Seoul National University, Seoul 151-744, Republic of Korea. [○]D. Son, J. Lee, and D. J. Lee contributed equally.

ABSTRACT Implantable endovascular devices such as bare metal, drug eluting, and bioresorbable stents have transformed interventional care by providing continuous structural and mechanical support to many peripheral, neural, and coronary arteries affected by blockage. Although effective in achieving immediate restoration of blood flow, the long-term re-endothelialization and inflammation induced by mechanical stents are difficult to diagnose or treat. Here we present nanomaterial designs and integration strategies for the bioresorbable electronic stent with drug-infused functionalized nanoparticles to enable flow sensing, temperature monitoring, data storage, wireless power/data transmission, inflammation suppression, localized drug delivery, and hyperthermia therapy. *In vivo* and *ex vivo* animal experiments as well as *in vitro* cell studies demonstrate the previously unrecognized potential for bioresorbable electronic implants coupled with bioinert therapeutic nanoparticles in the endovascular system.



KEYWORDS: bioresorbable · stent · transient electronics · flexible electronics · nanomedicine

Balloon angioplasty and stent placement procedures have helped shape patient care across a broad range of cardio-,¹ neuro-,² and peripheral³ vascular diseases. Approximately six million patients⁴ receive percutaneous coronary interventions (PCI) to treat arterial obstructions and endothelial injuries annually. While PCI using bare metal stents has been demonstrated to restore blood flow, there are key limitations whereby neointimal hyperplasia and smooth muscle cells (SMCs) may accumulate near the stent.⁵ These limitations are thought to arise from a complex interplay of turbulent blood flow and inflammatory reactions around the stent.^{1,5} To overcome drawbacks of bare metal stents, several approaches have been

reported, including bioresorbable stents⁶ and drug-eluting stents,⁷ which provide physical disappearance and deliver pharmacological agents, respectively, to mitigate risks of in-stent restenosis (ISR).

Although these existing classes of endovascular implants have enormous utility with minimal health risks, they do not provide diagnostic feedbacks on the state of hemodynamics and active controls of localized delivery of advanced therapeutic agents due to the absence of onboard sensors, data storage, and therapeutic actuation. Bioresorbable electronic stents that combine sensing of blood flow and temperature *via* integrated electronics coupled with data storage modules⁸ represent a

* Address correspondence to dskim98@snu.ac.kr, verocay@snuh.org, thyeon@snu.ac.kr.

Received for review January 29, 2015 and accepted April 23, 2015.

Published online April 23, 2015
10.1021/acs.nano.5b00651

© 2015 American Chemical Society

fundamentally new set of functionality onboard otherwise inert bioresorbable implants. High-performance flexible^{9–11} and bioresorbable^{12,13} electronics provide unique solutions for the integration of active electronics onto the inflatable and bioresorbable stent. In addition, advanced therapeutics *via* functionalized nanoparticles^{14–16} hold promise to further advance PEI through controlled drug release and long-term inflammation suppression. Inorganic nanoparticles have been explored as therapeutic platforms because of their high surface-to-volume ratio,¹⁷ ability to scavenge reactive oxygen species (ROS),¹⁸ and photoactivation properties.¹⁹

Here, we describe bioresorbable/bioinert nanomaterials designs and their integration strategies with a bioresorbable electronic stent (BES), fitted with nanomembrane-based flexible flow/temperature sensors and memory storage devices, anti-inflammatory nanoparticles, and drug-loaded core/shell nanospheres that are activated by an external optical stimulus. Additionally, antenna characteristics of BES for wireless power/data communication are evaluated. The mode of operation is as follows: the flow sensor measures blood flow, which is stored in the embedded memory module for pattern analysis and diagnosis. Catalytic ROS scavenging and hyperthermia-based drug release can be used as advanced therapies. First, the ceria nanoparticles (ceria NPs)²⁰ scavenge ROS generated in the perfusion by PEI and reduce inflammation that can cause in-stent thrombosis.²¹ Second, the gold nanorod core/mesoporous silica nanoparticle shell (AuNR@MSN)^{22,23} design is able to control the drug

loading and its release photothermally. The hyperthermia, which is regulated *via* feedback temperature sensing, controls localized drug delivery as well as provides thermal therapy. This suite of sensors and actuators provides mechanical, photothermal, diagnostic, and therapeutic functionality on bioresorbable stent substrates.

RESULTS AND DISCUSSION

Multifunctional Bioresorbable Electronic Stent. Figure 1a and b show a schematic diagram and a corresponding image of a representative bioresorbable electronic stent that includes a magnesium alloy stent integrated with ceria NPs (catalytic ROS scavenging), AuNR@MSN (photothermal therapy), drugs (*e.g.*, rapamycin, a well-known drug for the treatment of restenosis³ with some dysfunctions²⁴), flow/temperature sensors (physiological signal sensing), and an RRAM array (data storage). These components consist of bioresorbable and bioinert materials (see Figure 2a). Although the Mg alloy stent has rapid erosion problems,²⁵ the degradation time can be prolonged by multistacked encapsulation layers. Moreover, it is necessary to use a conductive Mg-based stent strut for the system, which acts as an antenna unit for wireless electronics. Details of the fabrication processes, materials, geometrical information, and images of the BES are included in the Supporting Information (SI), Figure S1. Figure 1b shows the BES (in deflated state) ready to be deployed in a canine common carotid artery *in vivo* *via* arterial access. The bottom inset is a magnified image of the BES, showing RRAM and a temperature sensor, coated

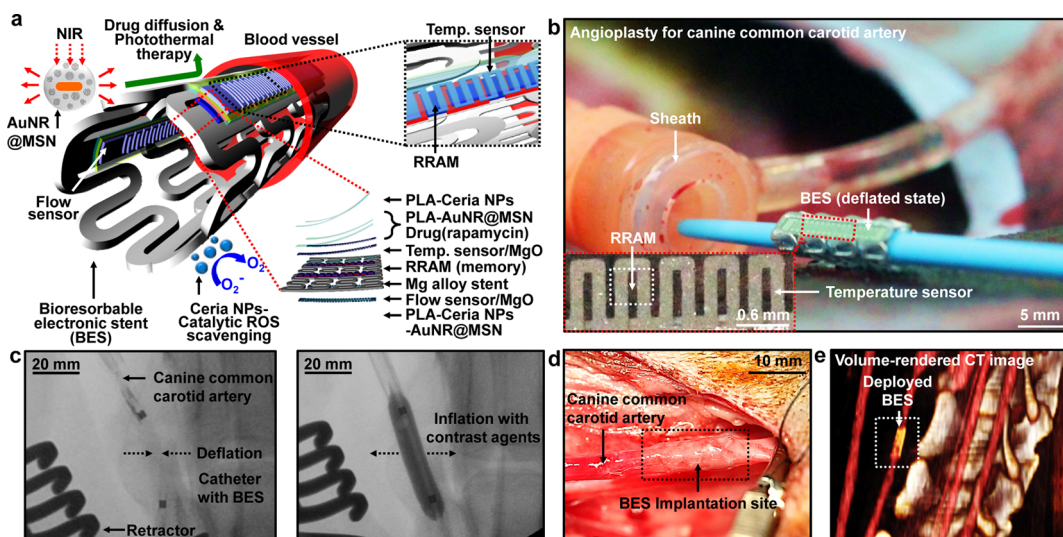


Figure 1. Bioresorbable electronic stent (BES). (a) Schematic illustration of the BES (left), its top view (top right), and the layer information (bottom right). The BES includes bioresorbable temperature/flow sensors, memory modules, and bioresorbable/bioinert therapeutic nanoparticles. The therapeutic functions are either passive (ROS scavenging) or actively actuated (hyperthermia-based drug release) by NIR exposure. (b) Image of the BES installed on the balloon catheter during the deployment into a canine common carotid artery *in vivo*. Inset (bottom) shows the RRAM (white dotted box) and the temperature sensor on the BES. (c) X-ray images of the balloon catheter and the BES in the canine model before (left) and after (right) the inflation of the balloon catheter. (d) Image of the deployed BES in the canine common carotid artery *in vivo*. (e) Volume-rendered X-ray computed tomography (CT) image of the deployed BES in the canine common carotid artery.

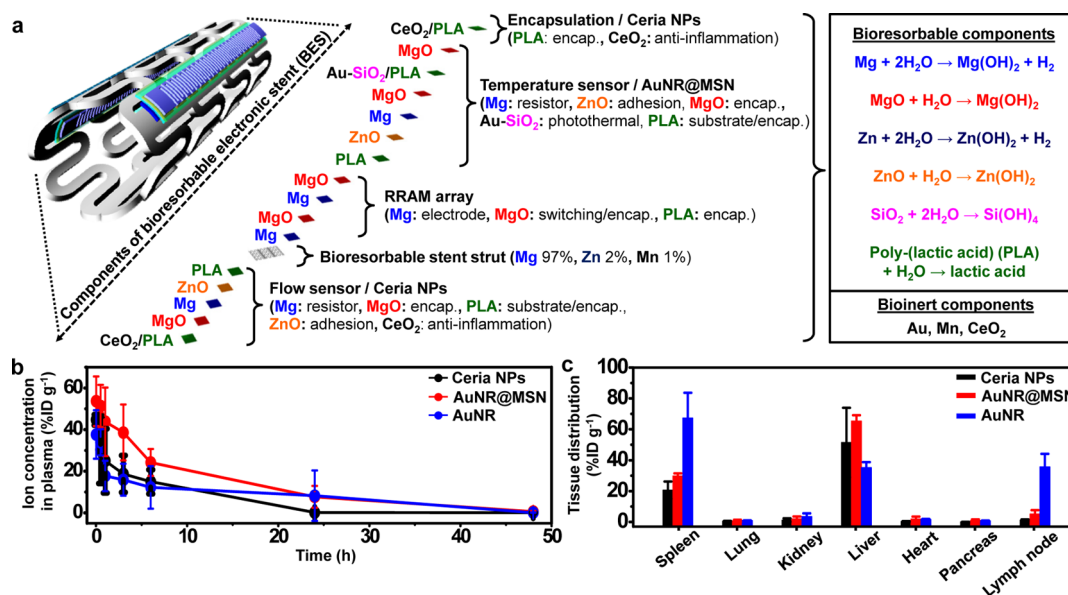


Figure 2. Bioreabsorbable and bioinert materials of the BES. (a) Bioreabsorbable and bioinert components of the BES, shown as an exploded view (left) and their hydrolysis (right). (b) Blood circulation data (ion concentration in plasma versus time) of ceria NP, AuNR@MSN, and AuNR injected into 8-week-old BALB/c mice ($n = 3$ for each nanoparticle group, 5 mg of Au or 2.5 mg of Ce per kg of mouse body weight). (c) Biodistribution profiles of ceria NP, AuNR@MSN, and AuNR injected into 8-week-old BALB/c mice ($n = 6$ for each nanoparticle group, 0.0625 mg of Ce or 0.125 mg of Au per mouse).

with nanoscale therapeutic agents. Figure 1c shows X-ray images of a deflated (left) and inflated (right) balloon catheter used to deploy the BES. The inflated BES mechanically supports the artery. An optical image (Figure 1d) and a volume-rendered computed tomography (CT) image (Figure 1e) highlight the expanded BES deployed inside the targeted artery.

Materials Biocompatibility and Structure of the Bioreabsorbable Electronic Stent. Most of bioreabsorbable stents for endovascular diseases lack multifunctionality, such as continuous monitoring, data storage, and instantaneous therapy, due to unavailability of integration processes of multifunctional device components. Specifically, the integration of bioreabsorbable active/passive devices on the stent has not been feasible, because the fabrication process of bioreabsorbable electronics is incompatible with the conventional microfabrication processes. Figure 2a shows an illustrative enumeration for bioreabsorbable and bioinert stacks of active electronics and therapeutic nanoparticles on a Mg–Zn–Mn alloy (ZM21; Mg 97%, Zn 2%, Mn 1%) strut. These electronic components consist of bioreabsorbable (Mg,^{12,26–28} MgO,^{12,27} Zn,^{26,28} ZnO,²⁹ and poly(lactic acid) (PLA)³⁰) and bioinert (Mn²⁸) materials (see Supporting Section 1.1). Therapeutic nanoparticles (ceria NPs and AuNR@MSN) and drugs are also incorporated in the PLA layers of the stent coated with dissolution-rate-controllable oxide/polymer, which plays a crucial role in reducing the fast corrosion rate of the stent strut and active electronic components (Figure S2a). All the used nanoparticles are either bioreabsorbable (SiO_2 ³¹) or bioinert (CeO_2 ,¹⁸ Au,³² see Supporting Section 1.1). The detailed average amount of each component is as

follows: 27.4 mg of ZM21 stent strut, 3.4 mg of electronic devices on PLA films, 0.51 mg of ceria nanoparticles, 0.16 mg of gold nanorod core, and 0.54 mg of silica shell. The amount of electronic devices on the stent is less than 0.1 mg. The rate of degradation of the active agents (in response to biofluid immersion) is illustrated in Figure S2b, which can be controlled by tuning the geometry and materials of encapsulating oxides (e.g., MgO) and polymers (e.g., PLA, silk^{33,34}).

Besides the bioreabsorbability, a key criterion for effective clinical treatments is the compatibility of bioinert nanomaterials with *in vivo* models. Although bioinert nanoparticles are slowly released from the PLA polymer, overdosed nanoparticles are used to confirm their biocompatibility. Bioinert nanoparticles in excess amounts (5 mg Au/kg and 2.5 mg Ce/kg) are injected through the tail vein of normal mice to evaluate the effect on the internal organs. See Supporting Section 1.2 for detailed experimental procedures. *In vivo* pharmacokinetic studies in mice show that ceria NPs, AuNR@MSN, and AuNR have half-lives of 1.9, 5.5, and 1.2 h (Figure 2b), which are similar to previous reports.³⁵ These results show that nanoparticles do not exhibit severe interactions with proteins and plaques that shorten half-lives in the bloodstream. Biodistribution studies show the accumulation of bioinert nanoparticles in the reticuloendothelial system such as the spleen, liver, and lymph node rather than in lung and other organs, as commonly observed^{36,37} (Figure 2c). The histological analysis (Figures S3 and S4, Supporting Section 1.2) shows the biocompatibility of nanoparticles.³⁸ These corroboratively show that the influence of bioinert nanoparticles on the *in vivo* system is minimal.

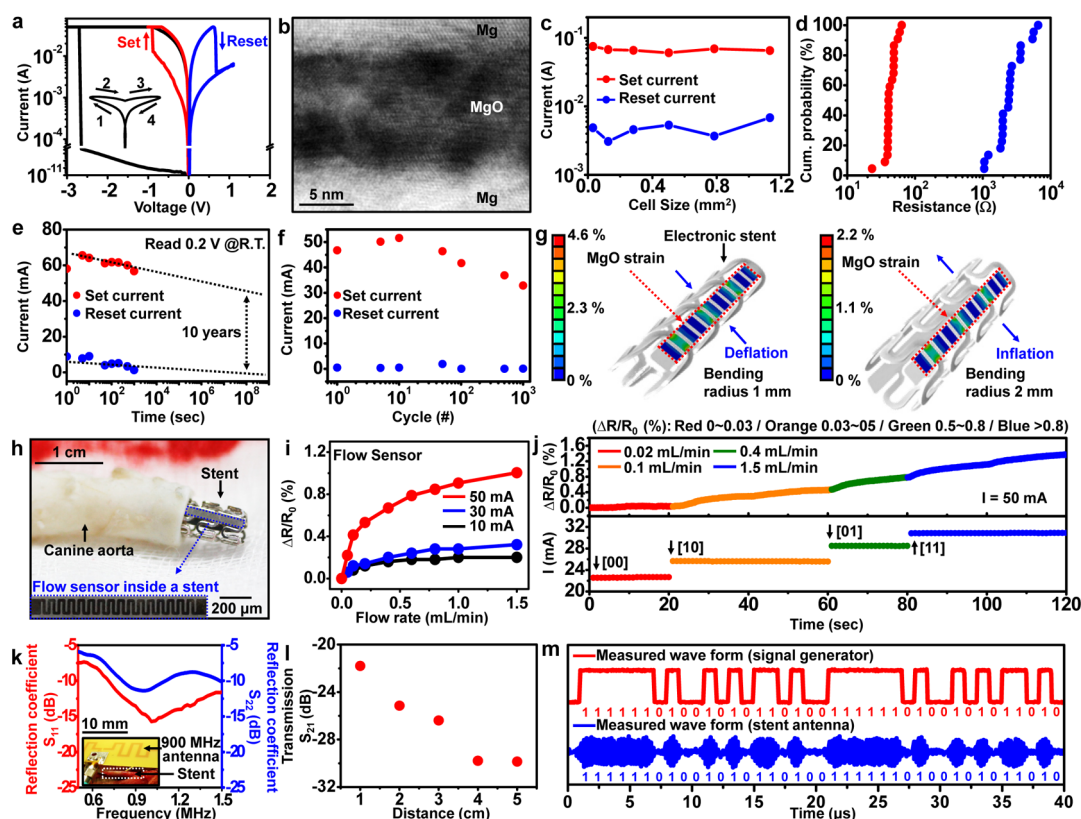


Figure 3. Electrical, mechanical, and wireless characteristics of the BES. (a) Current–voltage (I – V) characteristics of the bipolar resistance memory of the Mg/MgO/Mg structure. (b) Cross-sectional TEM image of the Mg/MgO/Mg memory cell. (c) Dependency of the set/reset current on the size of the memory cell. (d) Plot of the cumulative probability as a function of the set/reset resistance. (e) Retention characteristics of the memory. LRS and HRS current data are obtained at +0.2 V. (f) Endurance characteristics of the memory measured at +0.2 V. (g) Finite element modeling (FEM) of the strain distribution at the active layer (MgO) of the memory. (h) Image of the BES in the canine aorta for the *ex vivo* experiment of the blood flow sensing and the data storage in integrated memory devices. (i) Plot of the percent resistance change of the flow sensor *versus* the flow rates at three different current levels of the flow sensor. (j) Plot of the percent resistance change of the flow sensor (top) (measured with the 50 mA constant current). The measured flow rates are converted into digital signals and then stored into memory cells through the multilevel cell (MLC) operation. (k) Reflection coefficients of a stent antenna and a transmitting antenna in a canine common carotid artery *in vivo*. Inset image shows the wireless power/data experimental setup using a stent antenna and a transmitting antenna (900 MHz). (l) *In vivo* transmission coefficient S_{21} between a stent antenna and a transmitting antenna at different distances. (m) *In vivo* data transmission (1 Mbps) between a stent antenna and a transmitting antenna.

The mechanical strength and structural integrity of the bioresorbable stent mainly depend on the mechanical property of the stent strut. The current bioresorbable stent is composed of ZM21 alloy, which is known for its reliable corrosion resistance. The alloy that composes the strut can be changed with another Mg alloy (e.g., WE43) to further strengthen the mechanical and chemical properties. We found that the mechanical strength and structural integrity were maintained for a week *in vivo*.

Electrical Function of the Bioresorbable Electronic Stent.

Figure 3 shows results of active electronics in sensing and storing data from the BES. A bipolar I – V curve for the bioresorbable Mg/MgO/Mg nanomembrane resistance memory device shows how the device bidirectionally switches between a low-resistance state (LRS) and a high-resistance state (HRS) (Figure 3a). The resistive switching is achieved by applying a positive voltage (“reset” of 0.7 V) or a negative voltage (“set” of –0.8 V). The low reset and set voltages enable

low-power operations of the memory. The inset of Figure 3a shows the switching sequence. Figure 3b is a transmission electron microscope (TEM) image of a memory module, highlighting the MgO nanomembrane switch layer (~12 nm) and interfaces to Mg electrodes. A switching mechanism of the RRAM is detailed in Supporting Section 1.3. The area-independent current values for both the LRS and HRS suggest that the conducting mechanism is driven by the filamentary connection (Figure 3c).³⁹ The Mg/MgO/Mg RRAM is characterized by bipolar resistive switching behaviors typically observed in a memristor. Figure 3d shows uniform resistive switching in the RRAM array, where both the HRS and LRS are stable. The retention property of these devices can be extrapolated for up to several years (Figure 3e) with switching cycles exceeding 1000 times (Figure 3f). The multilevel cell (MLC) operation and its mechanism are shown in Figure S5a,b and c, respectively. Mechanical robustness during expansion of the BES is confirmed using finite element modeling

(FEM) analysis (see Supporting Section 1.4). We estimate the strain in the switching layer (MgO nanomembrane) of the BES (Figure 2g) to be less than the fracture strain of MgO ($\sim 8\%$).⁴⁰ Nanometer-thick active layers and serpentine designs incorporated in the BES (Figure S6a) minimize the effect of induced strains, and the flexibility is not affected, allowing for stable I – V characteristics under deformations (Figure S6b).

The bioresorbable RRAM is coupled with a sensor module on the BES in order to store sensing data. Figure 3h shows the BES in an *ex vivo* intravascular flow/perfusion model. A canine aorta (Figure 3h) is resected, and the BES is inserted in the path of simulated blood flow. The thermoresistive flow sensor on the stent is operated by measuring changes of resistance, which in turn correlate with changes in fluid velocity (Figure 3i). The RRAM modules store this flow data based on four-level data groups that correspond to flow rate changes. These rate changes are stored via the MLC operation (Figures 3j and S5). Each fluid velocity is stored in a different cell of the memory in real time by using the custom-made Labview software (Figure S7). Furthermore, the wall shear stress distributions, which are related to the restenosis process,⁴¹ are simulated by 3D computational fluid dynamics (CFD) (Figure S8, Supporting Section 1.5).

For wireless power/data transmission, we first investigate the reflection coefficients of a stent antenna at the port impedance of $50\ \Omega$ (Figure 3k). S_{11} of the BES strut at the telecommunication band (900 MHz) is -15 dB. Since the BES strut is composed of highly conductive magnesium alloy, the majority of the oscillating electric power is radiated to the external space, and thereby the stent strut can be used as the bioresorbable antenna.

With the stent and the transmitting antenna, the power transfer efficiency (S_{21}) from the transmission antenna to the stent antenna when they are separated by ~ 1 cm is -20.16 dB (*ex vivo*, Figure S9g) and -21.80 dB (*in vivo*, Figure 3l) at 900 MHz (detailed antenna characteristics and corresponding simulations for the analysis are included in the Supporting Section 1.6). S_{21} varies from -21.80 to -29.86 dB for a distance of 1–5 cm. The wireless data transmission is also tested. The 900 MHz ASK (amplitude shift keying) modulated pattern signal (1 Mbps) is generated and successfully transmitted to the BES antenna *ex vivo* (Figure S9h) and *in vivo* (Figure 3m). The power^{12,27,42} and the data^{43–45} can be transmitted more efficiently by impedance matching via the on-chip implementation of bioresorbable circuit components, such as lumped inductors and capacitors. In addition, more complex bioresorbable circuit components, such as rectifiers, oscillators, and modulators, can be integrated to establish the passive RF communications. A bioresorbable battery⁴⁶ can also be used for energy storage.

The BES equipped with functional sensors, memory modules, and wireless units is very important to facilitate practical PEI applications.

To deliver the therapy, we incorporated ceria NPs (Figure 4a and its inset for the magnified view) in the outermost encapsulation layer of the BES (Figures 1a and 4b left). Typically ROS near the implantation site promotes apoptosis of endothelial cells and ROS-induced inflammatory responses,^{20,47,48} one of major causes of restenosis. It also causes the death of cardiomyocytes.⁴⁸ The presence of oxygen vacancies on the surface of ceria NPs induces the binding of ROS to ceria NPs, and then self-regenerative redox cycles between Ce^{3+} and Ce^{4+} oxidation states¹⁸ allow the continuous catalytic scavenging of the endovascular ROS (Figure 4b right), suppressing ROS-induced inflammation. We used superoxide and hydrogen peroxide molecules to mimic increased ROS levels in cardiovascular systems during the angioplasty procedure.⁴⁸ Ceria NPs embedded in a PLA film exhibit ROS scavenging activity in a dose-dependent manner (Figure 4c).

Reactive Oxygen Species Scavenging Effect. We evaluated the antioxidative effects of ceria NPs *in vitro* by exposing human umbilical vein endothelial cells (HUVECs) to oxidative stresses (Figures 4d and S10). Once media containing ROS is added to the bath of the HUVECs, cell viability (in the absence of ceria NPs) decreases rapidly (Figure 4d, left, and e, black curve). In contrast, the addition of ceria NPs embedded in the PLA film improves the cell viability under oxidative stress (Figure 4d, right, and e, red curve), indicating endothelial cells are protected by ceria NPs from ROS. Exposure of cardiac muscle cell lines, HL-1, in conjunction with ceria NPs yields similar reduction in oxidative stress, as in HUVECs (Figure 4f and g). We investigated the protective effect of ceria NPs in animal models by assessing anti-inflammatory effects *in vivo*. Immunohistochemical analysis (Figure S11) following BES implantation in the canine common carotid artery shows the suppression of inflammatory responses and macrophage migration in the presence of ceria NPs (Figure 4h) without other therapeutic agents, whereas microphage recruitment is observed in the absence of ceria NPs (Figure 4i).

Hyperthermia-Based Controlled Drug Delivery. In addition to the protection against ROS and inflammation, multifunctional therapeutic nanoparticles responsive to external optical stimuli are also integrated on the BES to enable controlled drug release and photothermal therapy (Figure S12). Since drug-loaded nanoparticles are bound by PLA chains, the release rate is slow, and thereby continuous/controlled nanoparticle-based therapy over an extended period of time is possible. To achieve this form of actuation on the BES, we designed and synthesized nanoparticles containing a NIR-responsive AuNR core (~ 20 nm length and ~ 10 nm diameter) and drug-loadable mesoporous silica shell

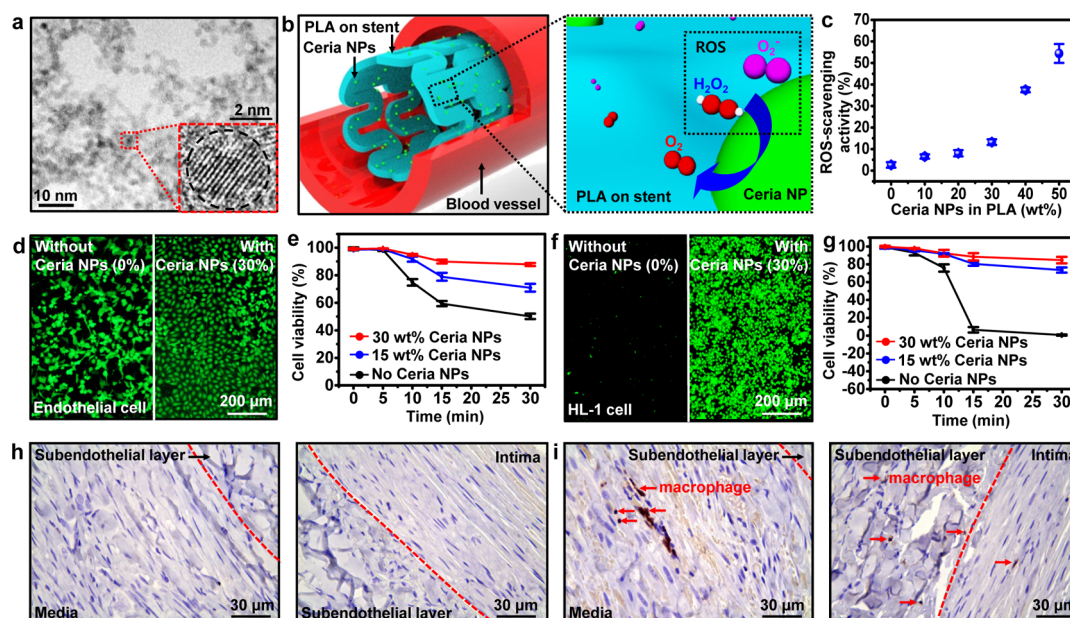


Figure 4. ROS scavenging effect of ceria NPs integrated on the BES. (a) TEM image of ceria NPs. The inset shows a magnified image by high-resolution TEM. (b) Schematic illustration of the ROS scavenging mechanism by ceria NPs. (c) Plot of the ROS scavenging activity of the ceria nanoparticle-embedded PLA film with different ceria concentrations (standard deviation from the mean, $n = 3$). The scavenging activity is measured by using the superoxide dismutase assay kit. (d) Fluorescent images of HUVECs under $50 \mu\text{M}$ ROS, without (left) and with (right) ceria NPs *in vitro*. (e) Cell viability of HUVECs with various ceria NP concentrations under $50 \mu\text{M}$ ROS (standard deviation from the mean, $n = 3$). (f) Fluorescent images of mouse cardiac muscle cells (HL-1) under $50 \mu\text{M}$ ROS, without (left) and with (right) ceria NPs *in vitro*. (g) Cell viability of HL-1 with various ceria NP concentrations under $50 \mu\text{M}$ ROS (standard deviation from the mean, $n = 3$). (h) *In vivo* immunolabeling image of MAC387 (macrophage) of the media and subendothelial layer (left) and subendothelial layer and intima (right) near the stent implantation site with ceria NPs. (i) *In vivo* immunolabeling image of MAC387 (macrophages) of the media and subendothelial layer (left) and subendothelial layer and intima (right) near the stent implantation site without ceria NPs.

(AuNR@MSN, diameters of ~ 100 nm) (Figure 5a; see the SI).^{22,23} The large surface area to volume ratio of AuNR@MSN⁴⁹ enables loading of large drug payloads (rapamycin, LC Laboratories, USA) to sustain the long-term medication for the suppression of SMC proliferation and restenosis.⁵⁰ To promote sufficient adsorption of large-molecular-sized drugs (rapamycin), we increased the size of the mesopore by adding swelling agents (mesitylene, Sigma-Aldrich, USA) (Figure S13a). N₂ adsorption/desorption isotherm analysis shows that AuNR@MSN has well-developed mesopores. The corresponding Barrett–Joyner–Halenda (BJH) pore size distribution indicates an effective pore diameter of ~ 3.9 nm (Figure S13b). The UV–vis adsorption spectrum indicates that AuNR@MSN has an adsorption peak at ~ 761 nm (Figure S13c). AuNR@MSN is responsive to a NIR laser (~ 800 nm) that has high penetration depth through soft tissue,^{22,23,51} and thereby it can be used for minimally invasive or noninvasive photothermal actuation of AuNR@MSN. Figure 5c highlights *in vitro* experiments of a drug release from AuNR@MSN in PLA with and without NIR laser (~ 800 nm) radiation. The AuNR core that absorbs NIR generates and transfers heat to the drug-loaded mesoporous silica shell, which, in turn, facilitates desorption and diffusion of loaded drug.^{22,23} By modulating the NIR laser power, we controlled the dosage of drug released (Figure 5b) from the BES. Although guiding the NIR beam through the

optical fiber to endovascular locations for photothermal therapies^{52,53} is still challenging, the drug delivery induced by guided-NIR was successfully demonstrated through *in vivo* experiments (Figures 5c and S14; see the SI for details). Furthermore, the radio frequency (RF) magnetic field can induce heat on the stent for accelerated drug diffusion (Figures S15 and S16; see the SI for details). The hyperthermia-based drug delivery from the stent to the intima is evaluated through the *in vivo* animal experiment (Figure 5d).

Integrated Temperature Sensing and Photothermal Therapy.

Thermal mapping at intravascular sites is important to ensure precise drug release and to prevent heat-induced cell necrosis. Because of the small areal coverage of the NIR laser spot on the temperature sensor ($\sim 18\%$ of total area of the temperature sensor; see Figure S17a in the SI for details), we applied a modified linear correlation ($\sim 0.014 \Omega/^{\circ}\text{C}$) for the temperature sensor (original correlation in Figure S17b). The photothermal experiment setup (Figure S17c) is further explained in the SI. To verify the effect of AuNR@MSN-based hyperthermia, we monitored the temperature relative to a control experiment (temperature sensor on the BES without AuNR@MSN). Results show a ~ 10 times increase in temperature changes by including AuNR@MSN (Figure 5e). The time-dependent and NIR-intensity-dependent temperature changes (monitored by the integrated temperature sensor) are shown in Figure S17d,e, respectively.

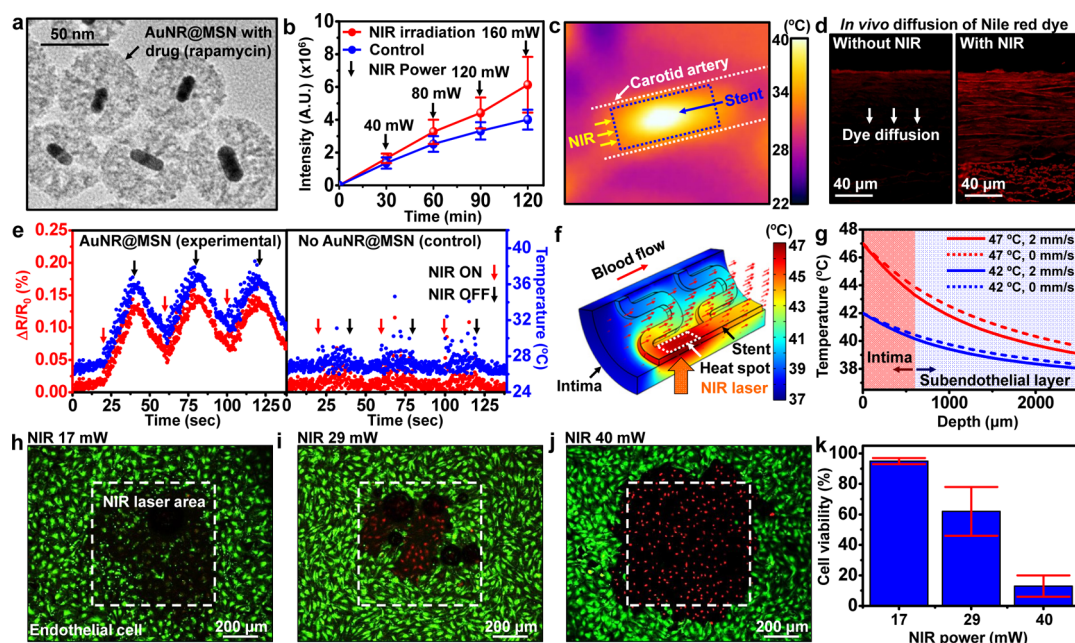


Figure 5. Hyperthermia-based controlled drug delivery, integrated temperature sensing, and photothermal therapy. (a) TEM image of the AuNR (core)/mesoporous silica (shell) with the antisthenosis drug (rapamycin). (b) Plot of fluorescent intensity as a function of time showing the simulated drug release experiment with fluorescein dyes loaded on AuNR@MSN under NIR laser irradiation (standard deviation from the mean, $n = 3$). (c) IR camera image of NIR-based hyperthermia effect on the stent inside a carotid artery. (d) Fluorescent images that show the diffused Nile Red dye (simulated drug) from the BES into the walls of the canine common carotid artery, without (left) and with (right) an optical-fiber-guided NIR laser. (e) Monitoring hyperthermia-induced temperature fluctuations on the BES with (left, experiment) and without (right, control) AuNR@MSN under intermittent NIR irradiation. (f) Thermal finite element modeling (FEM) of the temperature distribution near the stent/intima interface with a blood flow rate of 2 mm/s. The temperature at the heat spot (NIR laser spot) is assumed to be 47 °C. (g) Plot of the temperature distribution of the vascular tissues near the heated stent (intima and subendothelial layer) as a function of tissue depth, with (2 mm/s) and without (0 mm/s) blood flow, for two different temperature settings (42 and 47 °C). (h) Image of HUVECs on the PLA film containing AuNR@MSN. The NIR laser with 17 mW power is exposed in the white dotted box area *in vitro*. The green and red regions indicate live and dead cells, respectively. Photobleaching of the green dye is observed. (i) Image of HUVECs under NIR laser irradiation with increased power (29 mW). Dead cells (red color) due to the hyperthermia effect are observed. (j) Image of HUVECs under a NIR laser with 40 mW power. All cells exposed to the NIR laser are dead due to the hyperthermia effect of AuNR@MSN. (k) Cell viability data measured from Figure 4h–j.

The temperature distribution near the BES and in the adjacent intima region must be precisely controlled to prevent the generation of heat-induced clotting or endothelial cell death. Numerical thermal analysis (Figures 5f and S18) shows the three-dimensional thermal distribution near the heat focus area (~ 47 °C) generated by the NIR laser during occlusion (blood flow rate = 0 mm/s, Figure S18c) and reperfusion (blood flow rate = 2 mm/s, Figures 5f and S18d) conditions (see Supporting Section 1.7). Heating (maximum temperature ~ 47 °C) is significantly reduced by blood flow (Figure S18c,d), causing the blood temperature near the BES to remain below ~ 43 °C. The temperatures in the intima and subendothelial layers in direct contact with the stent decrease nonlinearly with depth. Blood flow at 2 mm/s helps to further reduce the tissue temperature slightly (Figure 5g). Considering the thickness of intima (~ 600 μm),⁵⁴ the heat conduction to cardiac tissues is tolerated without severe decrease of cell viability and mainly localized to the intima.

Figure 5h–j show fluorescence images of HUVECs after exposure to NIR laser radiation with discrete laser power and associated temperature change

(Figure S17d). HUVECs are dyed with Live/Dead viability/cytotoxicity kit (Life Technologies, USA), consisting of calcein-AM (green color, dye for live cells) and ethidium homodimer-1 (red color, dye for dead cells). When 17 mW of NIR laser power is applied for 10 min, HUVECs remain alive, with some detectable photobleaching of green dye by the laser (Figure 5h). However, cell death onset occurs (red-colored region) in response to 29 mW of NIR laser power (Figure 5i). As the NIR laser power is further increased to 40 mW, cell death expands to the surrounding region (Figure 5j). Quantitative analysis of cell viability as a function of laser power is shown in Figure 5k, which is consistent with the previous reports.⁵⁵ The utility of embedded temperature sensors on the BES can help mitigate cell injury and death during diagnosis and therapy. In addition, hyperthermia therapy is reported to prevent the accumulation of vulnerable plaques, which are prone to produce sudden risks, such as a heart attack or stroke.⁵⁶

CONCLUSION

The bioresorbable/bioinert nanomaterials, electronics, mechanics, and biomedical aspects of the BES

described in this study provide new opportunities for the integration of sensors, data storage elements, and optically responsive therapeutic nanoparticles for bioresorbable endovascular implants. This system with on-board bioresorbable sensors and memory modules resolves the limitations of existing stents by enabling the acquisition of physiological signals, data storage, anti-inflammation, localized drug delivery, and photothermal therapies through minimally invasive and/or noninvasive optical control. Numerical modeling and

FEM analysis validate the mechanical robustness of the active components and the thermal stability of hyperthermia-induced therapies using nanoparticles and lay the basis for future optimization of stent design. *In vitro*, *ex vivo*, and *in vivo* studies demonstrate the biocompatibility and multifunctional electronic and therapeutic utilities of the proposed biointegrated system. Further work will focus on the integration of wireless power^{12,27,42} and data communication^{43–45} in bioresorbable formats.

MATERIALS AND METHODS

Fabrication of Mg/MgO/Mg Memory on the Mg Alloy Stent. For the fabrication of Mg alloy stents, we first laser-cut and polish a ZM21 Mg alloy ingot. AZ4620 photoresist (Clariant, USA) is then spin-coated with 3000 rpm (for 30 s) on both sides of the ZM21 Mg alloy substrate (~200 μm). The Mg alloy substrate is then patterned using photolithography and wet etching processes with custom-made Mg etchant (70% ethylene glycol, 20% deionized water, 10% nitric acid). After the etching step, the Mg alloy mesh is dipped into boiling acetone to remove the AZ4620 photoresist. Then, an insulating MgO layer (~50 nm) is deposited on the stent by the electron beam evaporation. Thermal evaporation of Mg (~60 nm) is then applied to create the bottom electrode (base pressure of 1×10^{-6} Torr, ~0.5 $\text{\AA}/\text{s}$). The switching layer (MgO, 12 nm) is deposited *via* the sputtering process (base pressure of 5×10^{-6} Torr, Ar 20 sccm, 5 mTorr, 150 W RF power). Next, the top electrode (Mg, ~60 nm) is deposited onto the MgO film through another thermal evaporation step. Another encapsulating layer of MgO (~80 nm) is added to the top surface of the Mg/MgO/Mg (RRAM) construct using electron beam evaporation. Finally, the entire RRAM device on the stent is coated with PLA ($M_w \approx 160\,000$, $M_w/M_n \approx 1.5$, Sigma-Aldrich, USA) solution, containing ceria NPs and AuNR@MSN (3 wt % in chloroform) *via* a dip-coating technique.

Fabrication of Temperature/Flow Sensor on the Mg Alloy Stent. Mg temperature and flow sensors are composed of an adhesion layer, a long filamentary Mg resistor (sensing unit), and an outer encapsulation layer (MgO and PLA). First, the adhesion layer (~60 nm thick ZnO) is sputtered (base pressure of 5×10^{-6} Torr, Ar 20 sccm, 5 mTorr, 150 W RF power) on a ~15 μm thick PLA film. The metal line (Mg, ~100 nm) is thermally evaporated through a shadow mask. For encapsulation, ~400 nm thick MgO is deposited using electron beam evaporation. An additional two layers of PLA (~15 μm) are then laminated on top and exposed to chloroform vapor to make the PLA surface sticky. Finally, the sensor film is transfer-printed onto the sticky surface of the polymer on the stent.

***In Vitro* ROS Scavenging Experiment.** Mouse cardiac muscle cells (HL-1) are incubated in Claycomb medium (Sigma-Aldrich, USA) supplemented with 10% fetal bovine serum (Wisent, Canada), 1% penicillin/streptomycin (Gibco, USA), 0.1 mM norepinephrine (Sigma-Aldrich, USA), and 2 mM L-glutamine (Gibco, USA). Separately, HUVECs are incubated in an EGMTM-2 BulletKit (Lonza, Switzerland) at 37 $^{\circ}\text{C}$ with 5% CO_2 and 95% air. For *in vitro* ROS scavenging experiments, HL-1 cells and HUVECs are placed in 24-well plates and cultured again for 3 days. After removing the cell media, PLA film embedded with ceria NPs (1 $\text{cm} \times 1 \text{ cm}$, ~0.16 g) is placed in the well plate. Reactive oxygen species (50 μM H_2O_2 , Sigma-Aldrich, USA) are then added to well plates and stored for 5, 10, 15, and 30 min to see oxidative stress effects. Cells are washed with the Dulbecco's phosphate-buffered saline, and the cell viability is assessed with a Live/Dead Cell viability/cytotoxicity kit (Invitrogen, USA). Fluorescence images are captured with a fluorescence microscope (Nikon, Eclipse Ti, Japan), and the Image-Pro Plus software (MediaCybernetics, USA) kit provides quantitative estimates of living and necrotic cells.

***In Vitro* Hyperthermia Experiment.** To monitor the cell injury caused by hyperthermia, we first applied photothermal hyperthermic treatments to HUVECs cultured for 3 days in 24-well plates, in which AuNR@MSN-PLA film (5 mm \times 5 mm) is placed (Figure 5h–k). Cell viability/cytotoxicity kit solution is added to the media to visualize live and dead cells. For the photothermal hyperthermia treatment, 800 nm-pulsed laser light (Mai Tai eHP Deepsee, Spectra-Physics, USA) is delivered for 10 min at different powers with an irradiation area of 760 $\mu\text{m} \times 760 \mu\text{m}$. The average irradiance rates are in the range 1.7–4.0 W/cm^2 , and total energy is 1020–2400 J/cm^2 . After the NIR irradiation, cells are imaged using a confocal microscope (LSM-780, Carl Zeiss, Germany).

Conflict of Interest: The authors declare no competing financial interest.

Acknowledgment. This work was supported by IBS-R006-D1. D.-H.K. acknowledges the financial support from the Basic Science Research Program (2012R1A1A1004925) of the National Research Foundation of Korea (NRF) of the Ministry of Science, ICT, and Future Planning. This work was supported by the Seoul National University Research Grant. N. Lu acknowledges the NSF CMMI award under Grant No. 1301335.

Supporting Information Available: Detailed fabrication methods, experimental descriptions, additional analysis for RRAM, experimental information for *ex vivo*, *in vitro*, and *in vivo* analysis, modeling process for CFD, schematic illustration for drug delivery, and analysis for AuNR@MSN. The Supporting Information is available free of charge on the ACS Publications website at DOI: 10.1021/acs.nano.5b00651.

REFERENCES AND NOTES

- Serruys, P. W.; Kutryk, M. J. B.; Ong, A. T. L. Coronary-Artery Stents. *N. Eng. J. Med.* **2006**, *354*, 483–495.
- Zlokovic, B. V. Neurovascular Pathways to Neurodegeneration in Alzheimer's Disease and Other Disorders. *Nat. Rev. Neurosci.* **2011**, *12*, 723–738.
- Weinberg, M. D.; Lau, J. F.; Rosenfield, K.; Olin, J. W. Peripheral Artery Disease. Part 2: Medical and Endovascular Treatment. *Nat. Rev. Cardiol.* **2011**, *8*, 429–441.
- Howard-Alpe, G. M.; de Bono, J.; Hudsmith, L.; Orr, W. P.; Foex, P.; Sear, J. W. Coronary Artery Stents and Non-Cardiac Surgery. *Br. J. Anaesth.* **2007**, *98*, 560–574.
- Jukema, J. W.; Verschuren, J. J. W.; Ahmed, T. A. N.; Quax, P. H. A. Restenosis after PCI. Part 1: Pathophysiology and Risk Factors. *Nat. Rev. Cardiol.* **2012**, *9*, 53–62.
- Bertrand, O. F.; Sipehia, R.; Mongrain, R.; Rodés, J.; Tardif, J.-C.; Bilodeau, L.; Côté, G.; Bourassa, M. G. Biocompatibility Aspects of New Stent Technology. *J. Am. Coll. Cardiol.* **1998**, *32*, 562–571.
- Stefanini, G. G.; Holmes, D. R. Drug-Eluting Coronary-Artery Stents. *N. Eng. J. Med.* **2013**, *368*, 254–265.
- Son, D.; Lee, J.; Qiao, S.; Ghaffari, R.; Kim, J.; Lee, J. E.; Song, C.; Kim, S. J.; Lee, D. J.; Jun, S. W.; *et al.* Multifunctional Wearable Devices for Diagnosis and Therapy of Movement Disorders. *Nat. Nanotechnol.* **2014**, *9*, 397–404.

9. Kaltenbrunner, M.; Sekitani, T.; Reeder, J.; Yokota, T.; Kuribara, K.; Tokuhara, T.; Drack, M.; Schwödiauer, R.; Graz, I.; Bauer-Gogonea, S.; *et al.* An Ultra-Lightweight Design for Imperceptible Plastic Electronics. *Nature* **2013**, *499*, 458–463.
10. Sekitani, T.; Zschieschang, U.; Klauk, H.; Someya, T. Flexible Organic Transistors and Circuits with Extreme Bending Stability. *Nat. Mater.* **2010**, *9*, 1015–1022.
11. Viventi, J.; Kim, D.-H.; Vigeland, L.; Frechette, E. S.; Blanco, J. A.; Kim, Y.-S.; Avrin, A. E.; Tiruvadi, V. R.; Hwang, S.-W.; Vanleer, A. C.; *et al.* Flexible, Foldable, Actively Multiplexed, High-Density Electrode Array for Mapping Brain Activity *in Vivo*. *Nat. Neurosci.* **2011**, *14*, 1599–1605.
12. Hwang, S.-W.; Tao, H.; Kim, D.-H.; Cheng, H.; Song, J.-K.; Rill, E.; Brenckle, M. A.; Panilaitis, B.; Won, S. M.; Kim, Y.-S.; *et al.* A Physically Transient Form of Silicon Electronics. *Science* **2012**, *337*, 1640–1644.
13. Kim, D.-H.; Viventi, J.; Amsden, J. J.; Xiao, J.; Vigeland, L.; Kim, Y.-S.; Blanco, J. A.; Panilaitis, B.; Frechette, E. S.; Contreras, D.; *et al.* Dissolvable Films of Silk Fibroin for Ultrathin Conformal Bio-integrated Electronics. *Nat. Mater.* **2010**, *9*, 511–517.
14. Peer, D.; Karp, J. M.; Hong, S.; Farokhzad, O. C.; Margalit, R.; Langer, R. Nanocarriers as an Emerging Platform for Cancer Therapy. *Nat. Nanotechnol.* **2007**, *2*, 751–760.
15. Lohse, S. E.; Murphy, C. J. Applications of Colloidal Inorganic Nanoparticles: From Medicine to Energy. *J. Am. Chem. Soc.* **2012**, *134*, 15607–15620.
16. Mura, S.; Nicolas, J.; Couvreur, P. Stimuli-Responsive Nanocarriers for Drug Delivery. *Nat. Mater.* **2013**, *12*, 991–1003.
17. Vivero-Escoto, J.; Huxford-Phillips, R. C.; Lin, W. Silica-Based Nanoprobes for Biomedical Imaging and Theranostic Applications. *Chem. Soc. Rev.* **2012**, *41*, 2673–2685.
18. Karakoti, A.; Singh, S.; Dowding, J. M.; Self, W. T. Redox-Active Radical Scavenging Nanomaterials. *Chem. Soc. Rev.* **2010**, *39*, 4422–4432.
19. Huang, X.; El-Sayed, I. H.; Qian, W.; El-Sayed, M. A. Cancer Cell Imaging and Photothermal Therapy in the Near-Infrared Region by Using Gold Nanorods. *J. Am. Chem. Soc.* **2006**, *128*, 2115–2120.
20. Kim, C. K.; Kim, T.; Choi, I.-Y.; Soh, M.; Kim, D.; Kim, Y.-J.; Jang, H.; Yang, H.-S.; Kim, J. Y.; Park, H.-K.; *et al.* Ceria Nanoparticles that Can Protect Against Ischemic Stroke. *Angew. Chem., Int. Ed.* **2012**, *51*, 11039–11043.
21. Libby, P.; Simon, D. I. Inflammation and Thrombosis: The Clot Thickens. *Circulation* **2001**, *103*, 1718–1720.
22. Zhang, Z.; Wang, L.; Wang, J.; Jiang, X.; Li, X.; Hu, Z.; Ji, Y.; Wu, X.; Chen, C. Mesoporous Silica-Coated Gold Nanorods as a Light-Mediated Multifunctional Theranostic Platform for Cancer Treatment. *Adv. Mater.* **2012**, *24*, 1418–1423.
23. Yan, H.; Teh, S.; Sreejith, S.; Zhu, L.; Kwok, A.; Fang, W.; Ma, X.; Nguyen, K. T.; Korzh, V.; Zhao, Y. Functional Mesoporous Silica Nanoparticles for Photothermal-Controlled Drug Delivery *in Vivo*. *Angew. Chem., Int. Ed.* **2012**, *51*, 8373–8377.
24. Jabs, A.; Göbel, S.; Wenzel, P.; Kleschyov, A. L.; Hortmann, M.; Oelze, M.; Daiber, A.; Münzel, T. Sirolimus-Induced Vascular Dysfunction. *J. Am. Coll. Cardiol.* **2008**, *51*, 2130–2138.
25. Ormiston, J. A.; Serruys, P. W. S. Bioabsorbable Coronary Stents. *Circ.: Cardiovasc. Interventions* **2009**, *2*, 255–260.
26. Zberg, B.; Uggowitzer, P. J.; Löffler, J. F. MgZnCa Glasses without Clinically Observable Hydrogen Evolution for Biodegradable Implants. *Nat. Mater.* **2009**, *8*, 887–891.
27. Hwang, S.-W.; Huang, X.; Seo, J.-H.; Song, J.-K.; Kim, S.; Hage-Ali, S.; Chung, H.-J.; Tao, H.; Omenetto, F. G.; Ma, Z.; *et al.* Materials for Bioresorbable Radio Frequency Electronics. *Adv. Mater.* **2013**, *25*, 3526–3531.
28. Xu, L.; Yu, G.; Zhang, E.; Pan, F.; Yang, K. *In Vivo* Corrosion Behavior of Mg-Mn-Zn Alloy for Bone Implant Application. *J. Biomed. Mater. Res., Part A* **2007**, *83A*, 703–711.
29. Dagdeviren, C.; Hwang, S.-W.; Su, Y.; Kim, S.; Cheng, H.; Gur, O.; Haney, R.; Omenetto, F. G.; Huang, Y.; Rogers, J. A. Transient, Biocompatible Electronics and Energy Harvesters Based on ZnO. *Small* **2013**, *9*, 3398–3404.
30. Liu, X.; Jin, X.; Ma, P. X. Nanofibrous Hollow Microspheres Self-Assembled from Star-Shaped Polymers as Injectable Cell Carriers for Knee Repair. *Nat. Mater.* **2011**, *10*, 398–406.
31. Hwang, S.-W.; Park, G.; Cheng, H.; Song, J.-K.; Kang, S.-K.; Yin, L.; Kim, J.-H.; Omenetto, F. G.; Huang, Y.; Lee, K.-M.; *et al.* 25th Anniversary Article: Materials for High-Performance Biodegradable Semiconductor Devices. *Adv. Mater.* **2014**, *26*, 1992–2000.
32. Murphy, C. J.; Gole, A. M.; Stone, J. W.; Sisco, P. N.; Alkilany, A. M.; Goldsmith, E. C.; Baxter, S. C. Gold Nanoparticles in Biology: Beyond Toxicity to Cellular Imaging. *Acc. Chem. Res.* **2008**, *41*, 1721–1730.
33. Omenetto, F. G.; Kaplan, D. L. New Opportunities for an Ancient Material. *Science* **2010**, *329*, 528–531.
34. Kim, S.; Marelli, B.; Brenckle, M. A.; Mitropoulos, A. N.; Gil, E.-S.; Tsioris, K.; Tao, H.; Kaplan, D. L.; Omenetto, F. G. All-Water-Based Electron-Beam Lithography Using Silk as a Resist. *Nat. Nanotechnol.* **2014**, *9*, 306–310.
35. Huang, X.; Peng, X.; Wang, Y.; Wang, Y.; Shin, D. M.; El-Sayed, M. A.; Nie, S. A Reexamination of Active and Passive Tumor Targeting by Using Rod-Shaped Gold Nanocrystals and Covalently Conjugated Peptide Ligands. *ACS Nano* **2010**, *4*, 5887–5896.
36. Chen, Y.; Chen, H.; Shi, J. *In Vivo* Bio-Safety Evaluations and Diagnostic/Therapeutic Applications of Chemically Designed Mesoporous Silica Nanoparticles. *Adv. Mater.* **2013**, *25*, 3144–3176.
37. Yang, P.; Gai, S.; Lin, J. Functionalized Mesoporous Silica Materials for Controlled Drug Delivery. *Chem. Soc. Rev.* **2012**, *41*, 3679–3698.
38. Hirst, S. M.; Karakoti, A.; Singh, S.; Self, W.; Tyler, R.; Seal, S.; Reilly, C. M. Bio-Distribution and *in Vivo* Antioxidant Effects of Cerium Oxide Nanoparticles in Mice. *Environ. Toxicol.* **2013**, *28*, 107–118.
39. Kwon, D.-H.; Kim, K. M.; Jang, J. H.; Jeon, J. M.; Lee, M. H.; Kim, G. H.; Li, X.-S.; Park, G.-S.; Lee, B.; Han, S.; *et al.* Atomic Structure of Conducting Nanofilaments in TiO₂ Resistive Switching Memory. *Nat. Nanotechnol.* **2010**, *5*, 148–153.
40. Uchida, T.; Wang, Y.; Rivers, M. L.; Sutton, S. R. Yield Strength and Strain Hardening of MgO up to 8 GPa Measured in the Deformation-DIA with Monochromatic X-ray Diffraction. *Earth Planet. Sci. Lett.* **2004**, *226*, 117–126.
41. LaDisa, J. F.; Olson, L. E.; Molthen, R. C.; Hettrick, D. A.; Pratt, P. F.; Hardel, M. D.; Kersten, J. R.; Warltier, D. C.; Pagel, P. S. Alterations in Wall Shear Stress Predict Sites of Neointimal Hyperplasia after Stent Implantation in Rabbit Iliac Arteries. *Am. J. Physiol. Heart Circ. Physiol.* **2005**, *288*, H2465–H2475.
42. Sekitani, T.; Takamiya, M.; Noguchi, Y.; Nakano, S.; Kato, Y.; Sakurai, T.; Someya, T. A Large-Area Wireless Power-Transmission Sheet Using Printed Organic Transistors and Plastic MEMS Switches. *Nat. Mater.* **2007**, *6*, 413–417.
43. Chow, E. Y.; Chlebowski, A. L.; Chakraborty, S.; Chappell, W. J.; Irazoqui, P. P. Fully Wireless Implantable Cardiovascular Pressure Monitor Integrated with a Medical Stent. *Biomed. Eng. IEEE Trans.* **2010**, *57*, 1487–1496.
44. Tao, H.; Brenckle, M. A.; Yang, M.; Zhang, J.; Liu, M.; Siebert, S. M.; Averitt, R. D.; Mannoor, M. S.; McAlpine, M. C.; Rogers, J. A.; *et al.* Silk-Based Conformal, Adhesive, Edible Food Sensors. *Adv. Mater.* **2012**, *24*, 1067–1072.
45. Kim, T.-i.; McCall, J. G.; Jung, Y. H.; Huang, X.; Siuda, E. R.; Li, Y.; Song, J.; Song, Y. M.; Pao, H. A.; Kim, R.-H.; *et al.* Injectable, Cellular-Scale Optoelectronics with Applications for Wireless Optogenetics. *Science* **2013**, *340*, 211–216.
46. Yin, L.; Huang, X.; Xu, H.; Zhang, Y.; Lam, J.; Cheng, J.; Rogers, J. A. Materials, Designs, and Operational Characteristics for Fully Biodegradable Primary Batteries. *Adv. Mater.* **2014**, *26*, 3879–3884.
47. Juni, R. P.; Duckers, H. J.; Vanhoutte, P. M.; Virmani, R.; Moens, A. L. Oxidative Stress and Pathological Changes after Coronary Artery Interventions. *J. Am. Coll. Cardiol.* **2013**, *61*, 1471–1481.

48. Taniyama, Y.; Griendling, K. K. Reactive Oxygen Species in the Vasculature: Molecular and Cellular Mechanisms. *Hypertension* **2003**, *42*, 1075–1081.
49. Lee, J. E.; Lee, N.; Kim, T.; Kim, J.; Hyeon, T. Multifunctional Mesoporous Silica Nanocomposite Nanoparticles for Theranostic Applications. *Acc. Chem. Res.* **2011**, *44*, 893–902.
50. Kastrati, A.; Mehilli, J.; von Beckerath, N.; *et al.* Sirolimus-Eluting Stent or Paclitaxel-Eluting Stent vs Balloon Angioplasty for Prevention of Recurrences in Patients with Coronary In-Stent Restenosis: A Randomized Controlled Trial. *J. Am. Med. Assoc.* **2005**, *293*, 165–171.
51. Hirsch, L. R.; Stafford, R. J.; Bankson, J. A.; Sershen, S. R.; Rivera, B.; Price, R. E.; Hazle, J. D.; Halas, N. J.; West, J. L. Nanoshell-Mediated Near-Infrared Thermal Therapy of Tumors Under Magnetic Resonance Guidance. *Proc. Nat. Acad. Sci.* **2003**, *100*, 13549–13554.
52. Yeager, D.; Chen, Y.-S.; Litovsky, S.; Emelianov, S. Intravascular Photoacoustics for Image-Guidance and Temperature Monitoring during Plasmonic Photothermal Therapy of Atherosclerotic Plaques: A Feasibility Study. *Theranostics* **2014**, *4*, 36–46.
53. Yoo, H.; Kim, J. W.; Shishkov, M.; Namati, E.; Morse, T.; Shubochkin, R.; McCarthy, J. R.; Ntziachristos, V.; Bouma, B. E.; Jaffer, F. A.; *et al.* Intra-Arterial Catheter for Simultaneous Microstructural and Molecular Imaging *in Vivo*. *Nat. Med.* **2011**, *17*, 1680–1684.
54. de Groot, E.; Hovingh, G. K.; Wiegman, A.; Duriez, P.; Smit, A. J.; Fruchart, J.-C.; Kastelein, J. J. P. Measurement of Arterial Wall Thickness as a Surrogate Marker for Atherosclerosis. *Circulation* **2004**, *109*, III-33–III-38.
55. Brinton, M. R.; Tagge, C. A.; Stewart, R. J.; Cheung, A. K.; Shiu, Y.-T. E.; Christensen, D. A. Thermal Sensitivity of Endothelial Cells on Synthetic Vascular Graft Material. *Int. J. Hyperthermia* **2012**, *28*, 163–174.
56. Waxman, S.; Ishibashi, F.; Muller, J. E. Detection and Treatment of Vulnerable Plaques and Vulnerable Patients: Novel Approaches to Prevention of Coronary Events. *Circulation* **2006**, *114*, 2390–2411.